Journal of Applied Physics

Omnithermal metamaterials switchable between transparency and cloaking

Cite as: J. Appl. Phys. **128**, 095102 (2020); https://doi.org/10.1063/5.0013270
Submitted: 11 May 2020 . Accepted: 17 August 2020 . Published Online: 03 September 2020

Shuai Yang, Liujun Xu, Gaole Dai, and Jiping Huang

AIP Publishing

Journal of Applied Physics ARTICLE scitation.org/journal/jap

Omnithermal metamaterials switchable between transparency and cloaking

Cite as: J. Appl. Phys. **128**, 095102 (2020); doi: 10.1063/5.0013270
Submitted: 11 May 2020 · Accepted: 17 August 2020 ·
Published Online: 3 September 2020

View Online Export Citation CrossMark

Shuai Yang,[1,a)] Liujun Xu,[1] Gaole Dai,[2] and Jiping Huang[1,b)]

AFFILIATIONS

[1]Department of Physics, State Key Laboratory of Surface Physics, and Key Laboratory of Micro and Nano Photonic Structures (MOE), Fudan University, Shanghai 200438, China
[2]School of Sciences, Nantong University, Nantong 226019, China

Note: This paper is part of the Special Topic on Photothermics.
[a)]**Author to whom correspondence should be addressed:** syang18@fudan.edu.cn
[b)]**Electronic mail:** jphuang@fudan.edu.cn

ABSTRACT

Transparency and cloaking are two typical functions of thermal metamaterials that have attracted intensive research interest. However, two restrictions remain to be solved. The first one is that existing studies considered only one or two modes of heat transfer, which may not be consistent with practical conditions because conduction, radiation, and convection often coexist. The second one is that transparency and cloaking cannot be switched between at will. To solve these problems, we propose an effective medium theory to handle conductive, radiative, and convective (herein called omnithermal) processes simultaneously, which is based on the Fourier law, the Rosseland diffusion approximation, and the Darcy law. With the present theory, we further design an omnithermal metamaterial switchable between transparency and cloaking, which results from the nonlinear properties of radiation and convection. Finite-element simulations indicate that our scheme is robust under different boundary conditions. These results have potential applications such as in thermal camouflage, nonlinear thermotics, and intelligent thermotics.

I. INTRODUCTION

Thermal management is of particular significance to human beings. Since the proposal of transformation thermotics,[1,2] thermal metamaterials[3] with novel artificial structures have become a powerful tool to manipulate heat energy. A large number of thermal metamaterials were designed and fabricated to realize novel physical phenomena and practical applications, such as cloaking,[4–13] transparency,[14–17] and intelligent metamaterials.[18–21] However, these metamaterials focused on only one or two modes of heat transfer,[22–38] which may not be consistent with practical conditions because three methods of heat transfer (say, conduction, radiation, and convection) often coexist. Therefore, it is necessary to establish a theory to deal with conduction, radiation, and convection simultaneously, for example, by designing thermal metamaterials that can function under three heat transfer mechanisms.

In an attempt to solve this problem, we develop an effective medium theory to design omnithermal cloaking and transparency in this work. In detail, conduction is handled by the Fourier law, which is suitable for macroscopic thermal conduction, radiation is based on the Rosseland diffusion approximation, which is appropriate for a medium with a large optical thickness, and convection is handled with the Darcy law, which pertains to penetration models in porous media. The three modes correspond to three key parameters, the thermal conductivity κ, Rosseland mean extinction coefficient β, and permeability ς, which can be simultaneously calculated with the present theory. Based on the nonlinear properties of radiation and convection, we further propose a switchable omnithermal metamaterial that can adaptively switch functions between transparency [Fig. 1(a)] and cloaking [Fig. 1(b)] according to the temperature. Finite-element simulations are performed to show the feasibility of our scheme.

In Secs. II and III, we first confirm the functions of transparency and cloaking with theory and simulation. Then, we combine the two functions by taking advantage of nonlinear properties in order to design a switchable omnithermal metamaterial. Let us begin with the theory.

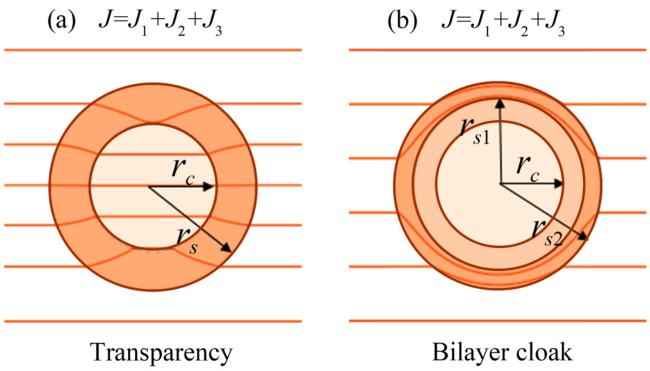

FIG. 1. Schematic diagrams of (a) transparency and (b) cloaking. Orange lines represent heat fluxes.

II. THEORY

If we consider all methods of heat transfer in a porous medium, then the passive and stable process of heat transfer is dominated by the Laplace equation,

$$\nabla \cdot \boldsymbol{J} = \nabla \cdot (\boldsymbol{J}_1 + \boldsymbol{J}_2 + \boldsymbol{J}_3) = 0, \tag{1}$$

where $\boldsymbol{J}$ is the total heat flux and its components, i.e., conductive flux $\boldsymbol{J}_1$, radiative flux $\boldsymbol{J}_2$, and convective flux $\boldsymbol{J}_3$, are given by the Fourier law, the Rosseland diffusion approximation, and the Darcy law, respectively,

$$\boldsymbol{J}_1 = -\kappa \nabla T, \tag{2}$$

$$\boldsymbol{J}_2 = -\gamma T^3 \nabla T, \tag{3}$$

$$\boldsymbol{J}_3 = \rho_f c_f \boldsymbol{v} T. \tag{4}$$

ρ_f and c_f are the density and heat capacity of the fluid. $\boldsymbol{v}$ represents the velocity of the fluid, which is given by the Darcy law $\boldsymbol{v} = -\varsigma/\eta_f \nabla P$, where ς is the permeability of the porous medium, η_f is the viscosity of the fluid, and P denotes pressure. κ is the thermal conductivity of the porous medium. γ $(=16\beta^{-1}n^2\sigma/3)$ is the radiative coefficient, where β is the Rosseland mean extinction coefficient, n is the relative refractive index, which is set to 1 throughout this work for brevity, and σ is the Stefan–Boltzmann constant $(=5.67 \times 10^{-8}\,\mathrm{W\,m^{-2}\,K^{-4}})$. The porous medium is composed of the solid and fluid; therefore, $\kappa = \phi\kappa_f + (1-\phi)\kappa_m$ and $\gamma = \phi\gamma_f + (1-\phi)\gamma_m$,[39] where ϕ is the porosity of the porous medium. κ_f (κ_m) and γ_f (γ_m) are the thermal conductivity and radiative coefficient of the fluid (solid), respectively. Here, we use the weighted mean model for the convenience of calculating and understanding. If more precise discussions are required, the Maxwell–Euken model is more suitable for the calculation of equivalent thermal conductivity of two-phase composites.

Although the heat-transfer process is dominated by many physical quantities, we care about three key physical quantities that correspond to the three methods of heat transfer, namely, the thermal conductivity κ, reciprocal of the Rosseland mean extinction coefficient β^{-1}, and the permeability ς.

Equation (1) can be rewritten as

$$\nabla \cdot \left(-\kappa \nabla T - \gamma T^3 \nabla T - \rho_f c_f \varsigma/\eta_f T \nabla P\right) = 0. \tag{5}$$

Then, two boundary conditions are considered: (I) the temperature field and pressure field are parallel and (II) the temperature field and pressure field are perpendicular.

For condition (I), the temperature field and pressure field are parallel in all regions (a detailed proof can be found in Appendix A). Therefore, it is reasonable to use a coordinate-dependent scalar function $f(r)$ to describe the relationship between ∇P and ∇T,

$$\nabla P = f(r)\nabla T. \tag{6}$$

Then, we can obtain

$$\nabla \cdot \left(-\kappa \nabla T - \gamma T^3 \nabla T - \rho_f c_f \varsigma/\eta_f T f(r) \nabla T\right) = 0. \tag{7}$$

Here, the ratios γ/κ and $\left(\rho_f c_f \varsigma/\eta_f\right)/\kappa$ of the core-shell structure should be two constants, namely, $\gamma/\kappa = \nu$ and $\left(\rho_f c_f \varsigma/\eta_f\right)/\kappa = \omega$. We can rewrite Eq. (5) as

$$\begin{aligned} &\nabla \cdot \left(-\kappa\left(1 + \nu T^3 + \omega T f(r)\right)\nabla T\right) \\ &= \nabla \cdot \left(-\kappa \nabla\left(T + \nu T^4/4 + F(r,\ T)\right)\right) = \nabla \cdot (-\kappa \nabla \varphi) = 0, \end{aligned} \tag{8}$$

where $\varphi = T + \nu T^4/4 + F(r,\ T)$ and $\nabla F(r,\ T) = \omega T f(r)\nabla T$. Since Eq. (8) is the Laplace equation, these three physical quantities (i.e., κ, β^{-1}, and ς) can be calculated with the effective medium theory.[18,19]

For the condition that the temperature field and the pressure field are perpendicular, Eq. (5) can be rewritten as

$$\begin{aligned} \nabla \cdot \left(-\kappa \nabla T - \gamma T^3 \nabla T\right) &= \rho_f c_f \nabla \cdot \left(\varsigma/\eta_f T \nabla P\right) \\ &= \rho_f c_f \nabla \cdot (-\boldsymbol{v} T) = -\rho_f c_f \boldsymbol{v} \cdot \nabla T, \end{aligned} \tag{9}$$

where we use the condition $\nabla \cdot \boldsymbol{v} = 0$ resulting from the mass conservation of thermal convection. The temperature field and velocity are perpendicular, yielding $\boldsymbol{v} \cdot \nabla T = 0$; therefore, the temperature field and the pressure field are decoupled. Then, the effective medium theory is still applicable based on the above discussion.

For omnithermal transparency [Fig. 1(a)], we suppose that the core with the radius r_c, the thermal conductivity κ_c, the Rosseland mean extinction coefficient β_c, and the permeability ς_c is coated by a shell with the corresponding parameters r_s, κ_s, β_s, and ς_s. Based on the effective medium theory, three effective values can be obtained,

$$\kappa_e = \kappa_s \frac{\kappa_c + \kappa_s + (\kappa_c - \kappa_s)p}{\kappa_c + \kappa_s - (\kappa_c - \kappa_s)p}, \tag{10}$$

$$\beta_e^{-1} = \beta_s^{-1} \frac{\beta_c^{-1} + \beta_s^{-1} + (\beta_c^{-1} - \beta_s^{-1})p}{\beta_c^{-1} + \beta_s^{-1} - (\beta_c^{-1} - \beta_s^{-1})p}, \tag{11}$$

$$\varsigma_e = \varsigma_s \frac{\varsigma_c + \varsigma_s + (\varsigma_c - \varsigma_s)p}{\varsigma_c + \varsigma_s - (\varsigma_c - \varsigma_s)p}, \tag{12}$$

where κ_e, β_e^{-1}, and ς_e represent the effective thermal conductivity, the effective reciprocal of the Rosseland mean extinction coefficient, and the effective permeability of the core-shell structure. $p = (r_c/r_s)^2$ is the area fraction.

For omnithermal cloaking [Fig. 1(b)], we take the core with radius r_c, thermal conductivity κ_c, reciprocal of the Rosseland mean extinction coefficient β_c^{-1}, and permeability ς_c coated by an inner shell with parameters r_{s1}, κ_{s1}, β_{s1}^{-1}, and ς_{s1} and an outer shell with parameters r_{s2}, κ_{s2}, β_{s2}^{-1}, and ς_{s2}. Bilayer cloaking requires the inner shell to be insulated; i.e., $\kappa_{s1} \to 0, \beta_{s1}^{-1} \to 0$, and $\varsigma_{s1} \to 0$. Then, we can derive

$$\kappa_e = \kappa_{s2} \frac{1-p}{1+p}, \tag{13}$$

$$\beta_e^{-1} = \beta_{s2}^{-1} \frac{1-p}{1+p}, \tag{14}$$

$$\varsigma_e = \varsigma_{s2} \frac{1-p}{1+p}, \tag{15}$$

where κ_e, β_e^{-1}, and ς_e are the effective thermal conductivity, the effective reciprocal of the Rosseland mean extinction coefficient, and the effective permeability of the core-shell-shell structure. $p = (r_{s1}/r_{s2})^2$ is the area fraction.

III. FINITE-ELEMENT SIMULATIONS

We then confirm the above theoretical models by performing finite-element simulations with COMSOL Multiphysics.[40] The parameters of the porous medium are $\kappa_f = 0.6\,\mathrm{W/(m\,K)}$, $\rho_f = 10^3\,\mathrm{kg/m^3}$, $c_f = 4.2 \times 10^3\,\mathrm{J/(kg\,K)}$, and $\eta_f = 10^{-3}\,\mathrm{Pa\,s}$. The porosity of the porous medium is $\phi = 0.1$. ρ_s and c_s are, respectively, set to be $10^3\,\mathrm{kg/m^3}$ and $10^3\,\mathrm{J/(kg\,K)}$ in what follows.

Figure 2 shows the simulation results with boundary condition (I). The simulation results for omnithermal transparency,

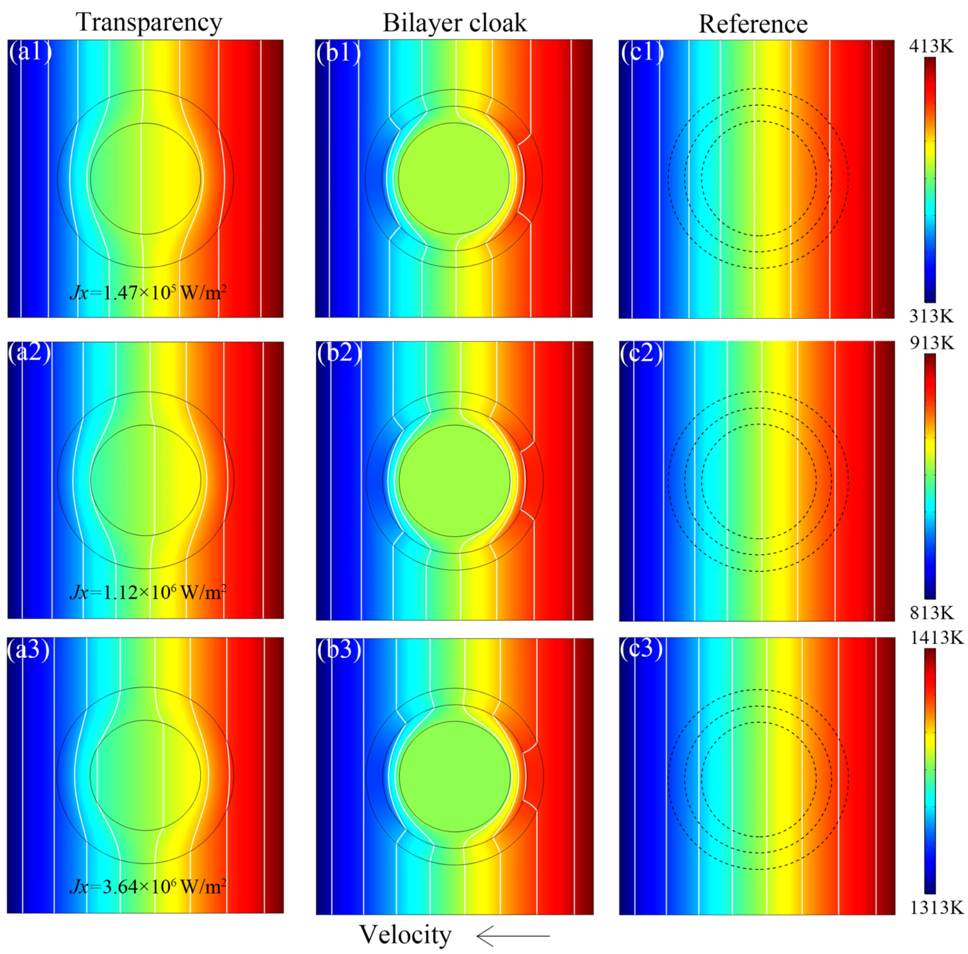

FIG. 2. Simulation results of (a1)–(a3) transparency, (b1)–(b3) cloaking, and (c1)–(c3) references with uniform fields. All simulation boxes are $10 \times 10\,\mathrm{cm^2}$. Other parameters are as follows. (a1)–(a3) $r_c = 2\,\mathrm{cm}$, $r_s = 3.2\,\mathrm{cm}$, $\kappa_c = 171\,\mathrm{W/(m\,K)}$, $\kappa_s = 43\,\mathrm{W/(m\,K)}$, $\kappa_b = 70\,\mathrm{W/(m\,K)}$, $\beta_c = 0.1\,\mathrm{m^{-1}}$, $\beta_s = 0.4\,\mathrm{m^{-1}}$, $\beta_b = 0.25\,\mathrm{m^{-1}}$, $\varsigma_c = 5\times 10^{-12}\,\mathrm{m^2}$, $\varsigma_s = 1.25 \times 10^{-12}\,\mathrm{m^2}$, and $\varsigma_b = 2 \times 10^{-12}\,\mathrm{m^2}$. (b1)–(b3) $r_c = 2\,\mathrm{cm}$, $r_{s1} = 2.6\,\mathrm{cm}$, $r_{s2} = 3.2\,\mathrm{cm}$, $\kappa_c = 360\,\mathrm{W/(m\,K)}$, $\kappa_{s2} = 342\,\mathrm{W/(m\,K)}$, $\kappa_b = 70\,\mathrm{W/(m\,K)}$, $\beta_c = 0.1\,\mathrm{m^{-1}}$, $\beta_{s2} = 0.05\,\mathrm{m^{-1}}$, $\beta_b = 0.25\,\mathrm{m^{-1}}$, $\varsigma_c = 5 \times 10^{-12}\,\mathrm{m^2}$, $\varsigma_{s2} = 9.8\times 10^{-12}\,\mathrm{m^2}$, and $\varsigma_b = 2 \times 10^{-12}\,\mathrm{m^2}$. (c1)–(c3) $\kappa = 70\,\mathrm{W/(m\,K)}$, $\beta = 0.25\,\mathrm{m^{-1}}$, and $\varsigma = 2 \times 10^{-12}\,\mathrm{m^2}$.

omnithermal cloaking, and references are presented in Figs. 2(a1)–2(a3), Figs. 2(b1)–2(b3), and Figs. 2(c1)–2(c3), respectively. The temperatures of the right and left boundaries are 413 and 313 K for Figs. 2(a1)–2(c1), 913 and 813 K for Figs. 2(a2)–2(c2), and 1413 and 1313 K for Figs. 2(a3)–2(c3). The pressures of the right and left boundaries in Figs. 2(a1)–2(c3) are 1000 and 0 Pa, respectively. For omnithermal transparency, the temperature distribution in the background should be the same as the reference, as if there was no a core-shell structure in the center. To ensure that omnithermal transparency works, we set $\kappa_b = \kappa_e$, $\beta_b^{-1} = \beta_e^{-1}$, and $\varsigma_b = \varsigma_e$ based on Eqs. (10)–(12). For bilayer cloaking, the cloaking region should be a constant temperature, and the temperature distribution in the background should not be disturbed. Thus, we set $\kappa_{s1} = 0.06\,\mathrm{W/(m\,K)}$, $\beta_{s1}^{-1} = 0.001\,\mathrm{m}$, and $\varsigma_{s1} = 10^{-15}\,\mathrm{m}^2$. Based on Eqs. (13)–(15), the properties of the background should be equal to the effective properties of the bilayer cloak: $\kappa_b = \kappa_e$, $\beta_b^{-1} = \beta_e^{-1}$, and $\varsigma_b = \varsigma_e$. The results of omnithermal transparency and cloaking conditions confirm the theory.

For boundary condition (II), we set the pressures of the bottom and top boundaries at 1000 and 0 Pa, respectively. The other conditions are kept unchanged. We perform simulations again with the new boundary conditions and obtain the corresponding results; see Fig. 3. Obviously, this change does not influence the effects of omnithermal transparency and cloaking.

Moreover, we apply a nonuniform thermal field to test the robustness of our scheme. The results are stable; see Fig. 4. In Figs. 4(a1)–4(c3), there is an elliptical source with high temperature and pressure at the bottom of the simulation box. We fix the upper boundary at 0 Pa and the source boundary at 1000 Pa. The other boundaries are insulated. The temperature settings are 413–313 K for Figs. 4(a1)–4(c1), 913–813 K for Figs. 4(a2)–4(c2), and 1413–1313 K for Figs. 4(a3)–4(c3). The other parameters are same as those for Fig. 2.

The Rosseland diffusion approximation suggests that the radiative flux $\boldsymbol{J}_2$ is proportional to T^3. The convective flux $\boldsymbol{J}_3$ is proportional to T, and the conductive flux $\boldsymbol{J}_1$ is independent of T. In Fig. 2, the directions of the radiative flux, conductive flux, and

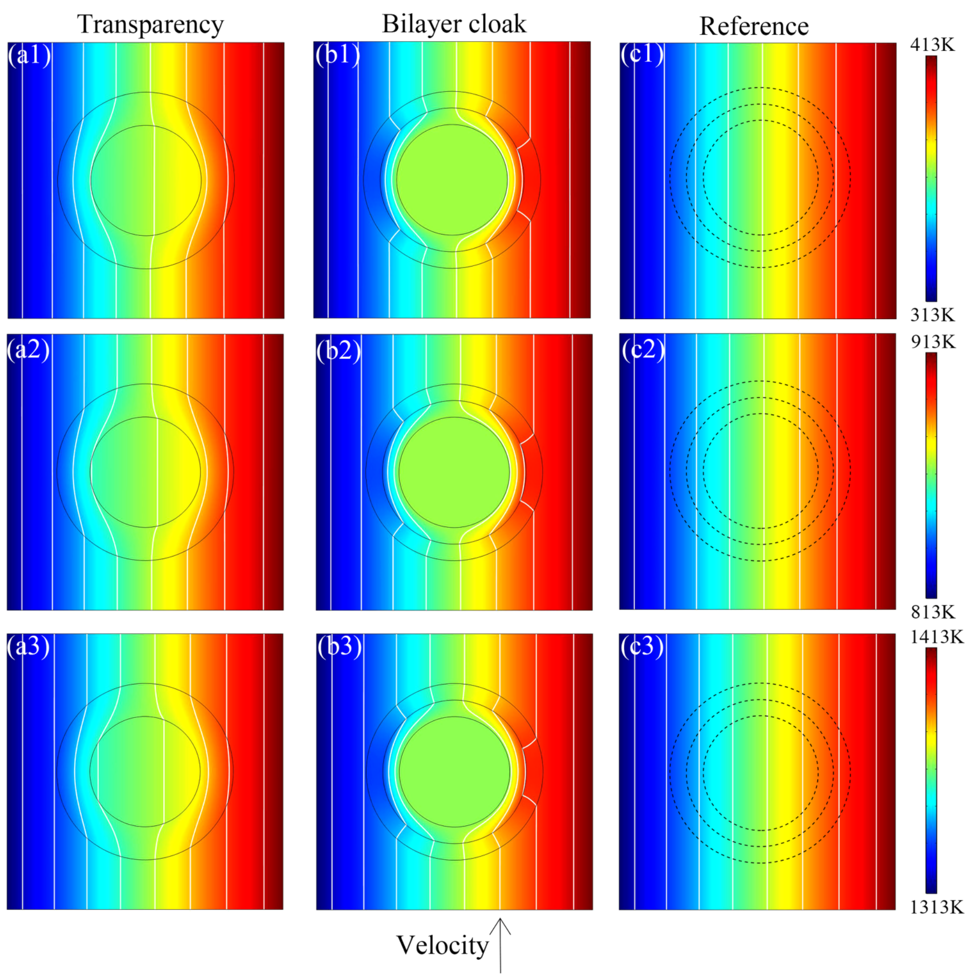

FIG. 3. Simulation results of (a1)–(a3) transparency, (b1)–(b3) cloaking, and (c1)–(c3) references with uniform fields. The pressures of the bottom and top boundaries are 1000 and 0 Pa, and the left and right boundaries are insulated. The other parameters are the same as those for Fig. 2.

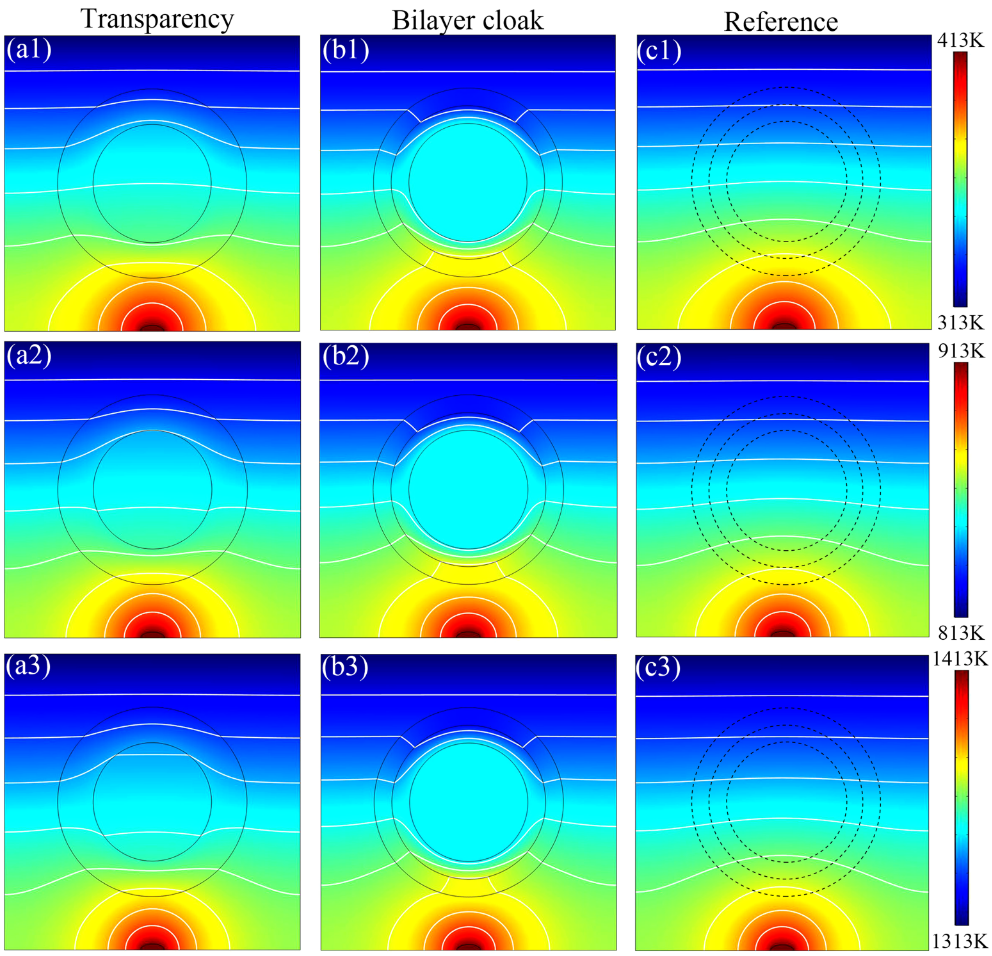

FIG. 4. Simulation results of (a1)–(a3) transparency, (b1)–(b3) cloaking, and (c1)–(c3) references with nonuniform fields. There is an elliptical source with high temperature and high pressure at the bottom of the simulation box. The other parameters are the same as those for Fig. 2.

convective flux are the same; therefore, the total flux $\boldsymbol{J}$ should have a positive correlation with T. We compare $\boldsymbol{J}$ in Figs. 2(a1)–2(a3) and find that $\boldsymbol{J}$ increases with increasing concrete temperature (the temperature difference remains unchanged). In other words, the radiative and convective effects increase with the increasing temperature.

With the nonlinear properties, we design a switchable omnithermal metamaterial; see Fig. 5(a). Existing thermal devices can hardly respond to external stimuli due to the lack of suitable mechanisms. Here, the nonlinear properties help us control the heat flux with temperature. When the device functions with a high temperature interval [Fig. 5(b)], bilayer cloaking is presented. When the device functions with a normal temperature interval [Fig. 5(c)], it switches to transparency. Different from the previous work, we introduce radiation and convection to achieve such an intelligent metamaterial that can adaptively switch its functions according to the external temperature. Actually, the switch between the different functions results from the competition between three mechanisms of heat transfer. Generally, thermal conduction is dominant at normal temperatures, and thermal convection and radiation are dominant at high temperatures. Therefore, we design the parameters related to thermal conduction to meet the requirements of transparency and design the parameters related to thermal convection and radiation to meet the requirements of bilayer cloaking. Then, the device can exhibit the cloaking function at high temperatures and the transparency function at normal temperatures. In addition to the temperature stimuli, the switchable functions can also be controlled by the pressure field. Although thermal conduction and radiation have no connection with the pressure field, thermal convection is dominated by the pressure. Therefore, the strength of convection can be controlled by the magnitude of the pressure field. Similarly, we can design the parameters related to thermal conduction and radiation to meet the requirements of one function and design the parameters related to thermal convection to meet the requirements of another function.

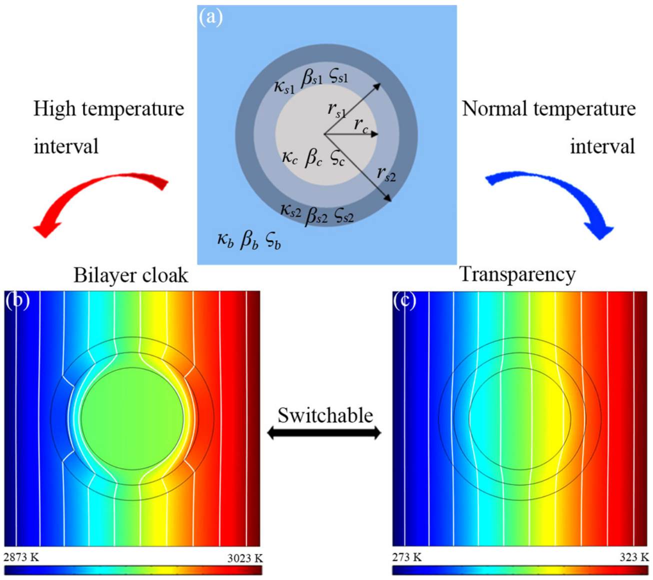

FIG. 5. Switchable omnithermal metamaterial. (a) Schematic diagram. (b) Bilayer cloak with a high temperature interval. (c) Transparency with a normal temperature interval. The pressures of the right and left boundaries are 1000 and 0 Pa, and the other boundaries are insulated. The other parameters are as follows: $r_c = 2\,\mathrm{cm}$, $r_{s1} = 2.6\,\mathrm{cm}$, $r_{s2} = 3.2\,\mathrm{cm}$, $\kappa_c = 35\,\mathrm{W/(m\,K)}$, $\kappa_{s1} = 20\,\mathrm{W/(m\,K)}$, $\kappa_{s2} = 20\,\mathrm{W/(m\,K)}$, $\kappa_b = 24.8\,\mathrm{W/(m\,K)}$, $\beta_c = 5\,\mathrm{m}^{-1}$, $\beta_{s1} = 1000\,\mathrm{m}^{-1}$, $\beta_{s2} = 2.04\,\mathrm{m}^{-1}$, $\beta_b = 10\,\mathrm{m}^{-1}$, $\varsigma_c = 5\times10^{-12}\,\mathrm{m}^2$, $\varsigma_{s1} = 10^{-15}\,\mathrm{m}^2$, $\varsigma_{s2} = 2.4\times10^{-12}\,\mathrm{m}^2$, and $\varsigma_b = 5\times10^{-13}\,\mathrm{m}^2$.

IV. DISCUSSION AND CONCLUSION

The above results consider a two-dimensional model, and they can also be extended to three-dimensional and noncircular cases; see Appendix B. A switchable device with other functions can be designed, such as concentrating and cloaking; see Appendix C. To make the convective properties clear, we also show the pressure distributions in Fig. 2 of Appendix D.

For experimental realization, we can resort to a quasi-two-dimensional porous medium as a practical structure whose thermal conductivity, radiative coefficient, and permeability can, in principle, be flexibly adjusted. For convection, common materials, such as air or water, can act as the carrier of convective flux. When designing a bilayer cloak, insulated materials, such as aerogels, are good candidates. The Rosseland diffusion approximation is appropriate for a medium with a large optical thickness. That is, the mean free path of photons is smaller than the system size; therefore, the propagation of photons can be treated as a diffusion process. Some materials, such as aerogels and glass, can be calculated with the Rosseland diffusion approximation. Although we neglect size effects in simulations, they should be considered in experiments to ensure that the fluid flow is laminar. As reported by recent studies,[41,42] we can also fabricate porous microfluidic metamaterials to control the convection process.

In this work, we mainly care about the temperature profiles in the background for transparency and cloaking. The difference is that transparency only requires a single layer; therefore, the temperature gradient is nonzero in the center. Certainly, this temperature gradient has a difference from that in the background, which results from the property of the effective medium theory. To reduce this difference, one may design a thinner shell.[16]

Actually, our theory is analytical. To fabricate thermal cloaking and transparency, we provide the relationship between the parameters of each component in the metamaterials by theoretical derivation; see Eqs. (10)–(15). Then, in the simulation section, we offer an example to validate the theory, and a set of parameters based on Eqs. (10)–(15) is selected for simulation. The accordance between the theory and simulations can be reflected by the temperature distribution and isotherms in the figures. Our approach can be used to design thermal metamaterials when the three heat transfer modes coexist and the thermal conductivities of the composites are temperature independent.

In summary, by developing an effective medium theory in omnithermotics, we can simultaneously manipulate three basic methods (conduction, radiation, and convection) of heat transfer in a porous medium. With the present theory, transparency and cloaking have been designed under different boundary conditions. Moreover, the nonlinear features of radiation and convection help us fabricate a switchable omnithermal metamaterial. We also extend the switchable device to other functions, such as concentrating and cloaking. Our scheme has potential applications in thermal camouflage,[43–47] thermal rectification,[48–50] and other intelligent metamaterials.

ACKNOWLEDGMENTS

We acknowledge the financial support by the National Natural Science Foundation of China (NNSFC) under Grant No. 11725521.

APPENDIX A: PROVING THAT THE PRESSURE FIELD AND THE TEMPERATURE FIELD ARE PARALLEL IN ALL REGIONS

We can derive the pressure and temperature distributions based on the boundary conditions if the ratio of the corresponding parameters of the core and shell is a constant. For the linear pressure field, we can obtain the general solutions of the pressure,

$$\begin{cases} P_b = A_1 r\cos\theta, \\ P_s = A_2 r\cos\theta + A_3 r^{-1}\cos\theta, \\ P_c = A_4 r\cos\theta, \end{cases} \tag{A1}$$

where P_b, P_s, and P_c represent the pressure of the matrix, shell, and core, respectively. A_1, A_2, A_3, and A_4 are all constants. The directions of the pressure gradient in all regions can be reflected by P_x/P_y. The subscript x (or y) denotes the differential with respect to x or y in what follows.

Similarly, for the nonlinear temperature field, the general solutions are

$$\begin{cases} \varphi(T)_b = BA_1 r\cos\theta, \\ \varphi(T)_s = BA_2 r\cos\theta + BA_3 r^{-1}\cos\theta, \\ \varphi(T)_c = BA_4 r\cos\theta, \end{cases} \tag{A2}$$

Journal of Applied Physics ARTICLE scitation.org/journal/jap

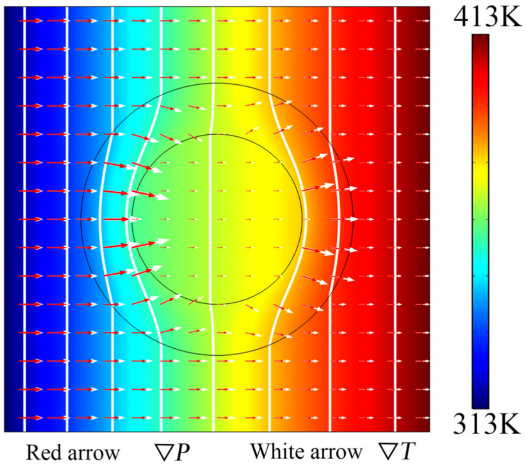

FIG. 6. Simulation result for transparency. The boundary conditions and parameters are the same as those for Fig. 2(a1). The red arrows indicate the pressure gradient (∇P), and the white arrows represent the temperature gradient (∇T).

where $\varphi(T)$ is a function of the temperature T, indicating that the temperature field is nonlinear. B is also a constant. Then, the directions of the temperature gradient in all regions can be reflected by $T_x/T_y = \varphi'(T)T_x/(\varphi'(T)T_y) = \varphi(T)_x/\varphi(T)_y$. Due to $P_x/P_y = T_x/T_y$, ∇T and ∇P are parallel.

Additionally, we also prove that the temperature field and the pressure field are parallel by a simulation; see Fig. 6. The difference between Figs. 6 and 2(a1) is that Fig. 6 plots the pressure gradient (∇P) with red arrows and the temperature gradient (∇T) with white arrows.

APPENDIX B: NONCIRCULAR SHAPE

Without loss of generality, we consider the three-dimensional ellipsoidal cases, which can be reduced to two dimensions with a simple operation. Similar to the previous discussion, for omnithermal transparency, we suppose that the core with semiaxis lengths r_{ci}, thermal conductivity κ_c, Rosseland mean extinction coefficient β_c, and permeability ς_c is coated by a shell with the corresponding parameters r_{si}, κ_s, β_s, and ς_s ($i = x,\ y,\ z$). The ellipsoid is confocal; therefore, r_{ci} and r_{si} are dependent. Based on the effective medium

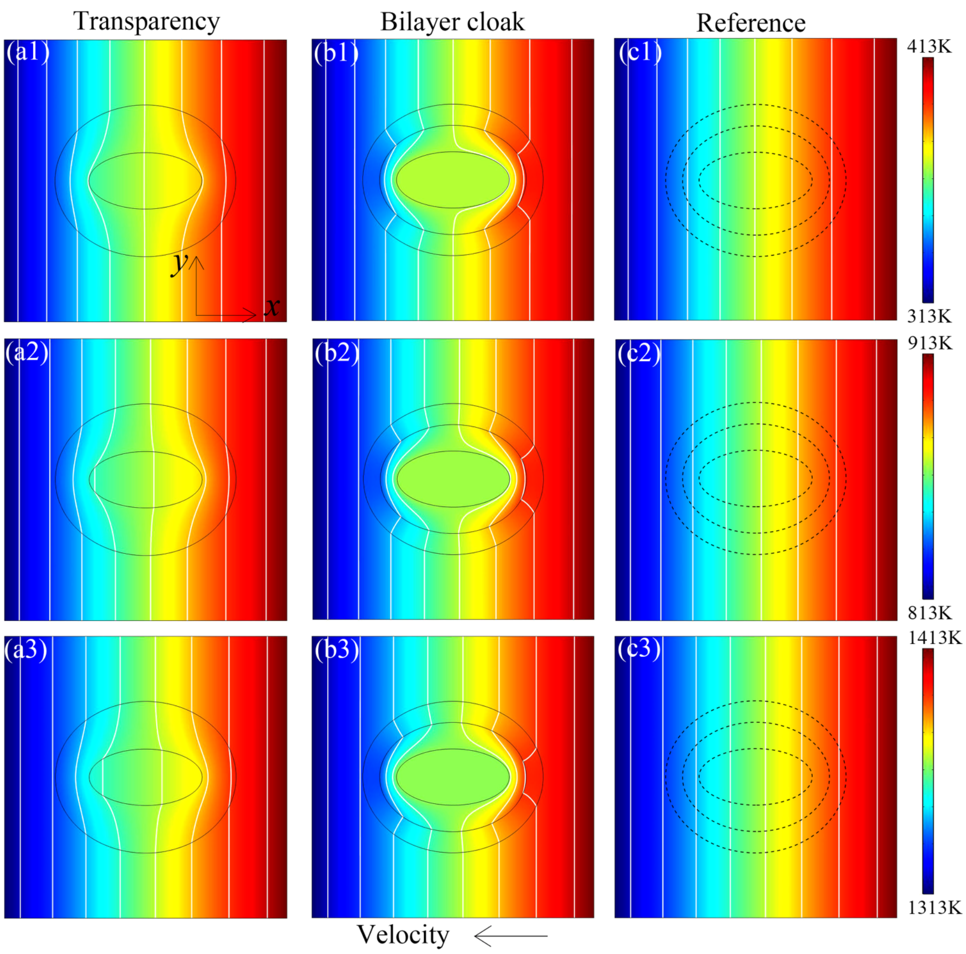

FIG. 7. Simulation results for (a1)–(a3) transparency, (b1)–(b3) cloaking, and (c1)–(c3) references with uniform fields. All of the simulation boxes are $10\times10\,\mathrm{cm}^2$. The other parameters are as follows. (a1)–(a3) r_{cx}=2cm, r_{cy}=1cm, r_{sx}=3.2cm, r_{sy}=2.69cm, κ_c=200W/(mK), κ_s=50W/(mK), κ_b=70.7W/(mK), β_c=0.1m^{-1}, β_s=0.4m^{-1}, β_b=0.28m^{-1}, ς_c=5×10^{-12}m^2, ς_s=1.25×10^{-12}m^2, and ς_b=1.77×10^{-12}m^2. (b1)–(b3) r_{cx}=2cm, r_{cy}=1cm, r_{s1x}=2.6cm, r_{s1y}=1.94cm, r_{s2x}=3.2cm, r_{s2y}=2.69cm, κ_c=360W/(mK), κ_{s1}=0.06W/(mK), κ_{s2}=200W/(mK), κ_b=60.5W/(mK), β_c=0.1m^{-1}, β_{s1}=1000m^{-1}, β_{s2}=0.05m^{-1}, β_b=0.17m^{-1}, ς_c=5×10^{-12}m^2, ς_{s1}=10^{-15}m^2, ς_{s2}=1.25×10^{-12}m^2, and ς_b=3.78×10^{-13}m^2. (c1)–(c3) κ=70.7W/(mK), β=0.28m^{-1}, and ς=1.77×10^{-12}m^2.

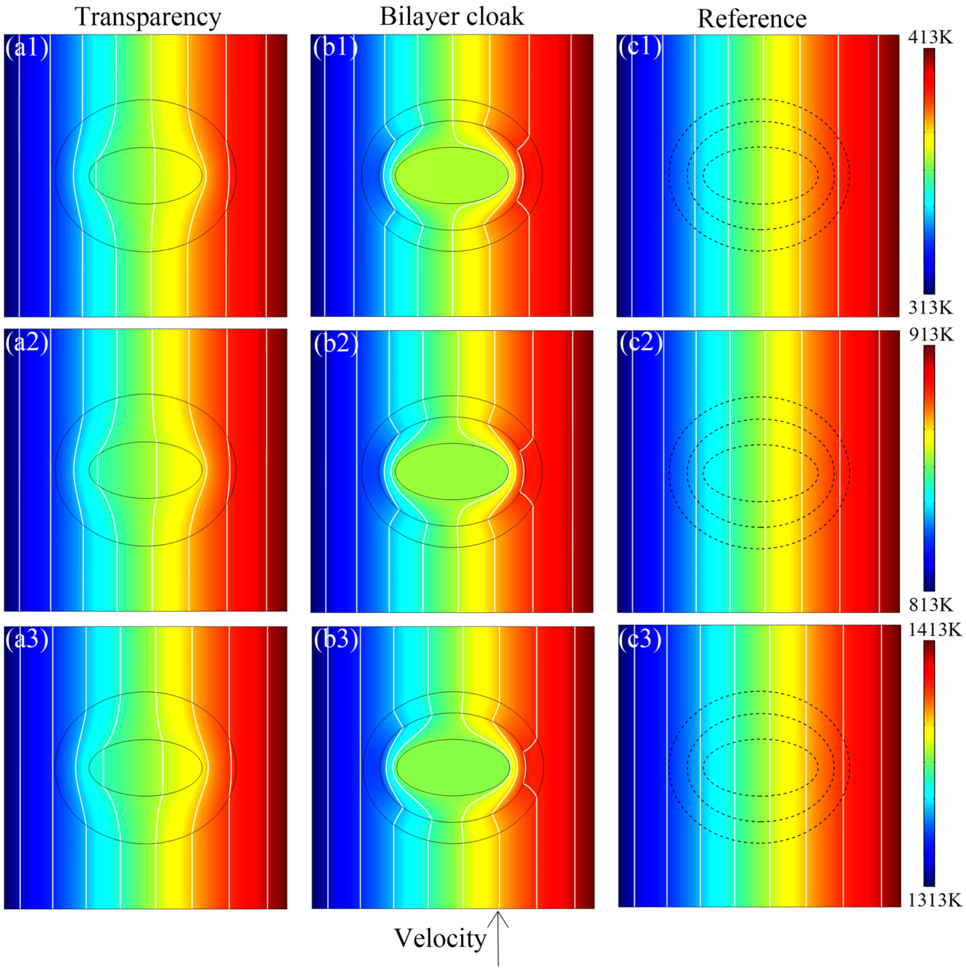

FIG. 8. Simulation results with uniform fields. The pressures of the bottom and top boundaries are 1000 and 0 Pa, and the left and right boundaries are insulated. (a1)–(a3) $\varsigma_b = 1.58 \times 10^{-12}\,\mathrm{m}^2$. (b1)–(b3) $\varsigma_b = 2.68 \times 10^{-13}\,\mathrm{m}^2$. (c1)–(c3) $\varsigma = 1.58 \times 10^{-12}\,\mathrm{m}^2$. The other parameters are the same as those for Fig. 7.

theory,[51] we can obtain

$$\kappa_{ei} = \kappa_s\left[\frac{(\kappa_c - \kappa_s)p}{\kappa_s + (f_{ci} - pf_{si})(\kappa_c - \kappa_s)} + 1\right], \tag{B1}$$

$$\beta_{ei}^{-1} = \beta_s^{-1}\left[\frac{(\beta_c^{-1} - \beta_s^{-1})p}{\beta_s^{-1} + (f_{ci} - pf_{si})(\beta_c^{-1} - \beta_s^{-1})} + 1\right], \tag{B2}$$

$$\varsigma_{ei} = \varsigma_s\left[\frac{(\varsigma_c - \varsigma_s)p}{\varsigma_s + (f_{ci} - pf_{si})(\varsigma_c - \varsigma_s)} + 1\right], \tag{B3}$$

where κ_{ei}, β_{ei}^{-1}, and ς_{ei} are the effective thermal conductivity, the effective reciprocal of the Rosseland mean extinction coefficient, and the effective permeability of the core-shell structure along the i direction. $p = r_{cx}r_{cy}r_{cz}/r_{sx}r_{sy}r_{sz}$ is the volume fraction. f_{ci} and f_{si} are the shape factors of the core and shell along the i direction, which can be calculated as

$$f_{ci} = \frac{r_{cx}r_{cy}r_{cz}}{2}\int_0^\infty \left(\alpha + r_{ci}^2\right)^{-1}\left[\left(\alpha + r_{cx}^2\right)\left(\alpha + r_{cy}^2\right)\left(\alpha + r_{cz}^2\right)\right]^{-1/2} d\alpha, \tag{B4}$$

$$f_{si} = \frac{r_{sx}r_{sy}r_{sz}}{2}\int_0^\infty \left(\alpha + r_{si}^2\right)^{-1}\left[\left(\alpha + r_{sx}^2\right)\left(\alpha + r_{sy}^2\right)\left(\alpha + r_{sz}^2\right)\right]^{-1/2} d\alpha. \tag{B5}$$

For bilayer cloaking, the effective thermal conductivity κ_{ei}, the effective reciprocal of the Rosseland mean extinction coefficient β_{ei}^{-1}, and the effective permeability ς_{ei} of the core-shell-shell structure along the i direction can be derived as

$$\kappa_{ei} = \kappa_{s2}\left[\frac{p}{f_{s1i} - pf_{s2i} - 1} + 1\right], \tag{B6}$$

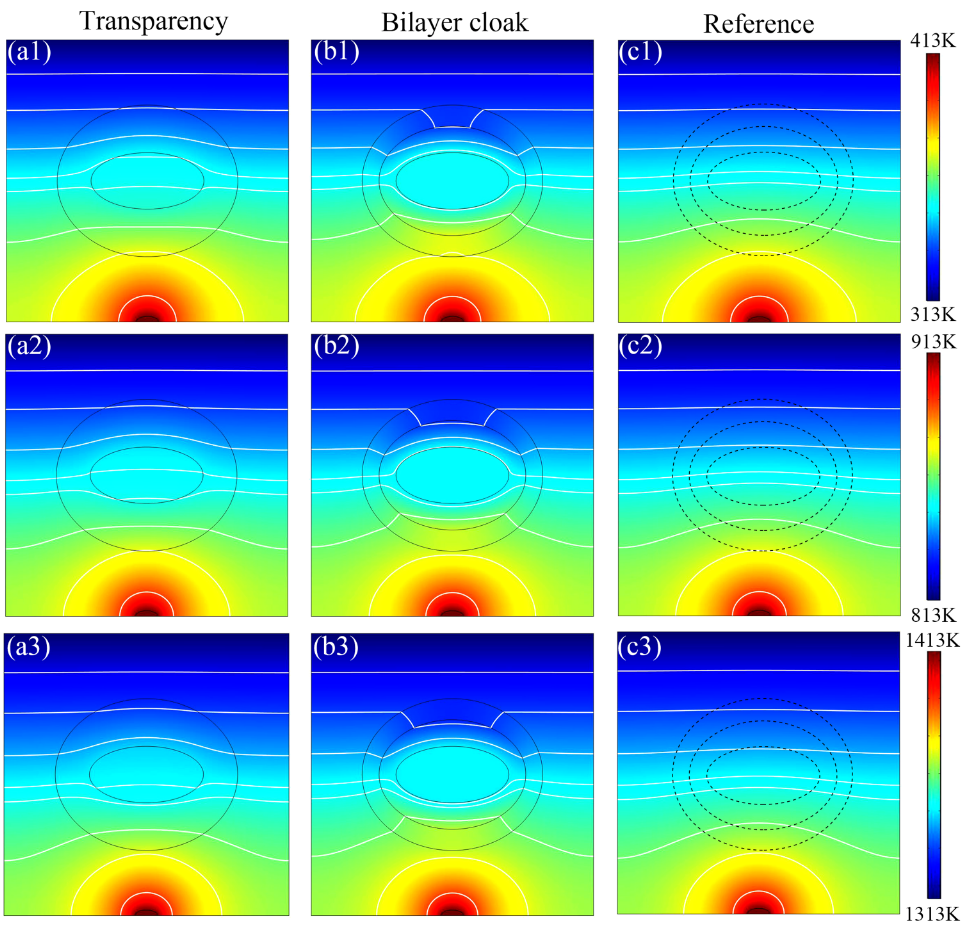

FIG. 9. Simulation results with nonuniform fields. There is an elliptical source with high temperature and pressure at the bottom of the simulation box. (a1)–(a3) κ_b=63.3W/(mK), β_b=0.32m^{-1}, and ς_b=1.58×10^{-12}m^2. (b1)–(b3) κ_b=42.8W/(mK), β_b=0.23m^{-1}, and ς_b=2.68×10^{-13}m^2. (c1)–(c3) κ=63.3W/(mK), β=0.32m^{-1}, and ς=1.58×10^{-12}m^2. The other parameters are the same as those for Fig. 7.

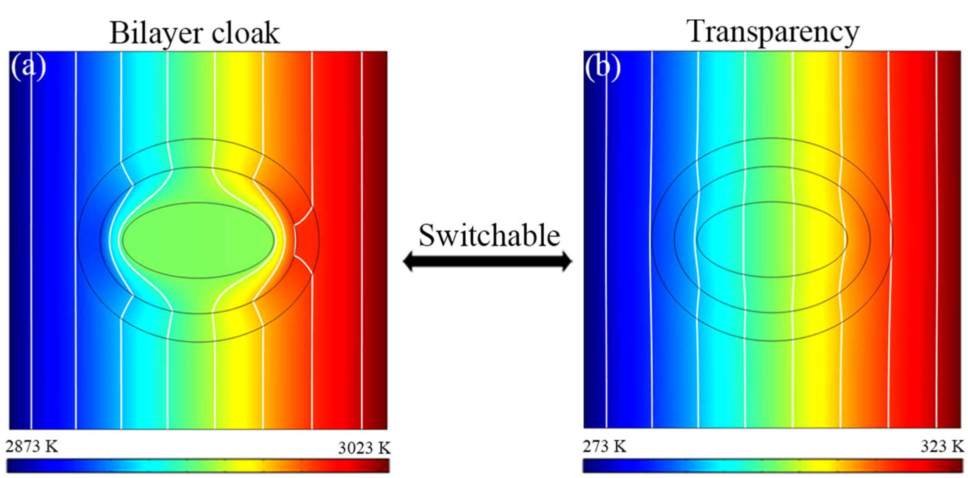

FIG. 10. A switchable omnithermal metamaterial. (a) A bilayer cloak. (b) A transparency device. The pressures of the right and left boundaries are 1000 and 0 Pa, and the other boundaries are insulated. The other parameters are as follows: $r_{cx} = 2$ cm, $r_{cy} = 1$ cm, $r_{s1x} = 2.6$ cm, $r_{s1y} = 1.94$ cm, $r_{s2x} = 3.2$ cm, $r_{s2y} = 2.69$ cm, $\kappa_c = 400$ W/(m K), $\kappa_{s1} = 320$ W/(m K), $\kappa_{s2} = 320$ W/(m K), $\kappa_b = 337.6$ W/(m K), $\beta_c = 0.1$ m^{-1}, $\beta_{s1} = 1000$ m^{-1}, $\beta_{s2} = 0.05$ m^{-1}, $\beta_b = 0.17$ m^{-1}, $\varsigma_c = 5\times 10^{-12}$ m^2, $\varsigma_{s1} = 10^{-15}$ m^2, $\varsigma_{s2} = 1.25 \times 10^{-12}$ m^2, and $\varsigma_b = 3.78\times 10^{-13}$ m^2.

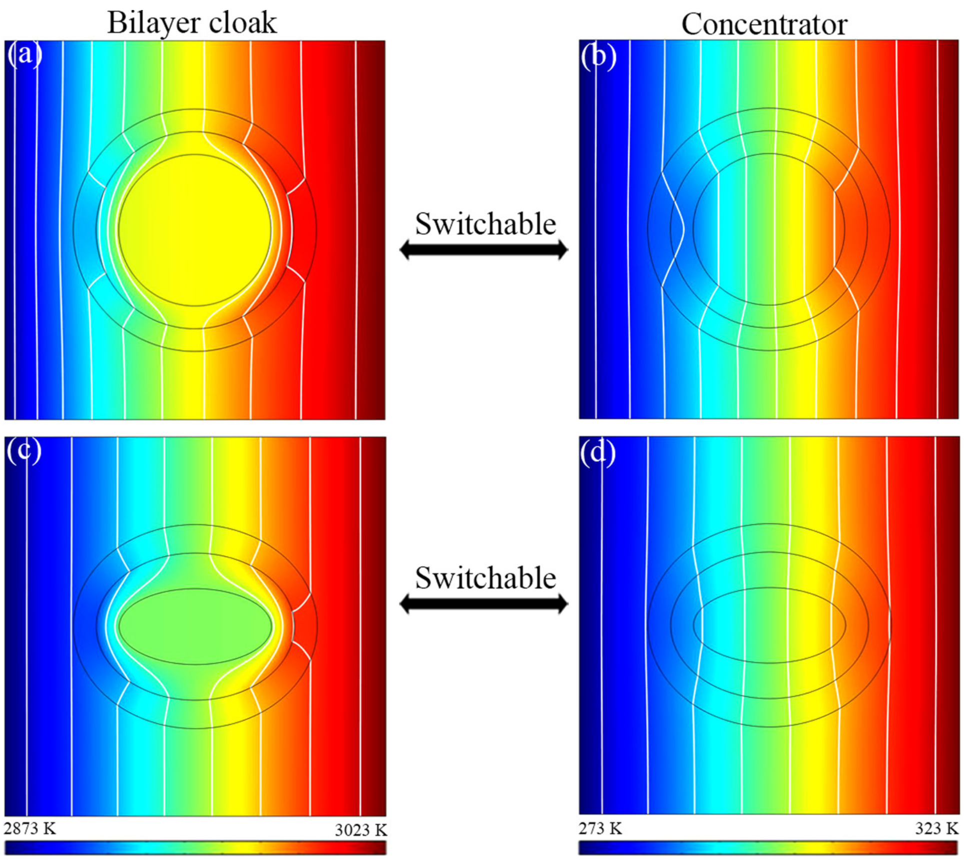

FIG. 11. Switchable omnithermal metamaterials. (a) and (c) A bilayer cloak. (b) and (d) A concentrator. The pressures of the right and left boundaries are 1000 and 0 Pa, and the other boundaries are insulated. The other parameters are as follows: (a) and (b) $r_c = 2$ cm, $r_{s1} = 2.6$ cm, $r_{s2} = 3.2$ cm, $\kappa_c = 1$ W/(m K), $\kappa_{s1} = 20$ W/(m K), $\kappa_{s2} = 20$ W/(m K), $\kappa_b = 9.6$ W/(m K), $\beta_c = 5$ m^{-1}, $\beta_{s1} = 1000$ m^{-1}, $\beta_{s2} = 2.04$ m^{-1}, $\beta_b = 10$ m^{-1}, $\varsigma_c = 5\times 10^{-12}$ m^2, $\varsigma_{s1} = 10^{-15}$ m^2, $\varsigma_{s2} = 2.4\times 10^{-12}$ m^2, and $\varsigma_b = 5\times 10^{-13}$ m^2. (c) and (d) $r_{cx} = 2$ cm, $r_{cy} = 1$ cm, $r_{s1x} = 2.6$ cm, $r_{s1y} = 1.94$ cm, $r_{s2x} = 3.2$ cm, $r_{s2y} = 2.69$ cm, $\kappa_c = 150$ W/(m K), $\kappa_{s1} = 360$ W/(m K), $\kappa_{s2} = 360$ W/(m K), $\kappa_b = 303.75$ W/(m K), $\beta_c = 0.1$ m^{-1}, $\beta_{s1} = 1000$ m^{-1}, $\beta_{s2} = 0.05$ m^{-1}, $\beta_b = 0.17$ m^{-1}, $\varsigma_c = 5\times 10^{-12}$ m^2, $\varsigma_{s1} = 10^{-15}$ m^2, $\varsigma_{s2} = 1.25\times 10^{-12}$ m^2, and $\varsigma_b = 3.78\times 10^{-13}$ m^2.

$$\beta_{ei}^{-1} = \beta_{s2}^{-1}\left[\frac{p}{f_{s1i} - pf_{s2i} - 1} + 1\right], \tag{B7}$$

$$\varsigma_{ei} = \varsigma_{s2}\left[\frac{p}{f_{s1i} - pf_{s2i} - 1} + 1\right], \tag{B8}$$

where $p = r_{s1x}r_{s1y}r_{s1z}/r_{s2x}r_{s2y}r_{s2z}$ is the volume fraction. f_{s1i} and f_{s2i} are the shape factors of the inner and outer shells along the i direction.

This is a theory for three-dimension confocal cases. It can also be reduced to two dimensions. Concretely speaking, the expressions [Eqs. (B1)–(B3)] and [Eqs. (B6)–(B8)] are unchanged, but the calculations of p and f change. In two dimensions, p is the area fraction; therefore, it is expressed as $p = r_{cx}r_{cy}/r_{sx}r_{sy}$. The shape factors have a reduced form of $f_{cx} = r_{cy}/(r_{cx} + r_{cy})$, $f_{cy} = r_{cx}/(r_{cx} + r_{cy})$, $f_{cz} = 0$, $f_{sx} = r_{sy}/(r_{sx} + r_{sy})$, $f_{sy} = r_{sx}/(r_{sx} + r_{sy})$, and $f_{sz} = 0$.

For accordance with the main text, we still perform finite-element simulations in two dimensions and extend Figs. 2–5 to the elliptical cases. Since Figs. 7–10 in Appendix B correspond to

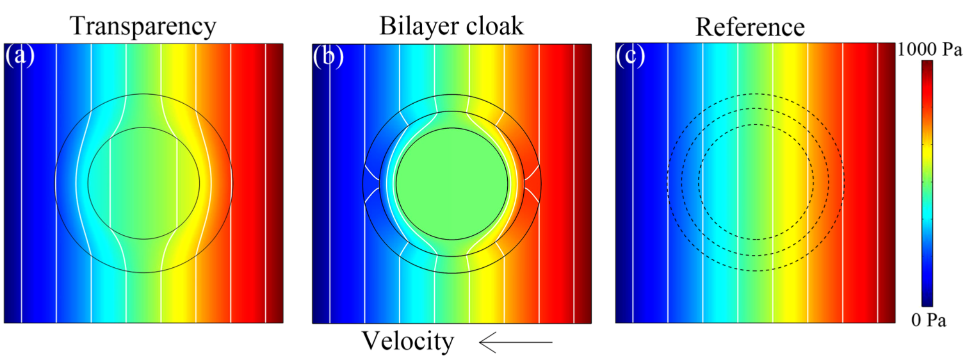

FIG. 12. Simulation results for (a) transparency, (b) cloaking, and (c) references. The boundary conditions and parameters are the same as those for Fig. 2. The color surface indicates the pressure distributions, and the white lines represent the isobaric lines in Fig. 12.

Figs. 2–5 in the main, respectively, we discuss them briefly. Except for Fig. 9, the figures correspond to uniform applied fields. We directly set the background parameters to be the effective values along the directions of the respective physical fields, although the effective values are essentially anisotropic. This is not appropriate for nonuniform fields; therefore, the background parameters in Fig. 9 should be anisotropic. We take the values of the effective parameters along the y direction for consistency and convenience. The functions can still work well. The simulation results confirm our theoretical models. For circular and elliptical cases, the effective medium theory is applicable. However, it cannot strictly handle the cases with complex shapes; therefore, the method of coordinate transformation is still a powerful tool that can help us design various metamaterials.

APPENDIX C: DEVICE SWITCHABLE BETWEEN CLOAKING AND CONCENTRATING

Besides the switchable functions between transparency and cloaking, we also extend the switchable device to other functions, such as concentrating and cloaking; see Fig. 11. The circular cases [Figs. 11(a) and 11(b)] and the elliptical cases [Figs. 11(c) and 11(d)] act as thermal cloaking at high temperatures and become thermally concentrating at normal temperatures.

APPENDIX D: PRESSURE DISTRIBUTIONS

We also plot the pressure distributions for transparency, cloaking, and references; see Fig. 12. Since the temperature does not affect the pressure distributions, permeability becomes the only related parameter.

DATA AVAILABILITY

The data support the findings of this study are available within the article.

REFERENCES

[1] C. Z. Fan, Y. Gao, and J. P. Huang, "Shaped graded materials with an apparent negative thermal conductivity," Appl. Phys. Lett. **92**, 251907 (2008).

[2] T. Y. Chen, C. N. Weng, and J. S. Chen, "Cloak for curvilinearly anisotropic media in conduction," Appl. Phys. Lett. **93**, 114103 (2008).

[3] J. P. Huang, "Thermal metamaterials make it possible to control the flow of heat at will," ES Energy Environ. **6**, 1 (2020).

[4] J. Y. Li, Y. Gao, and J. P. Huang, "A bifunctional cloak using transformation media," J. Appl. Phys. **108**, 074504 (2010).

[5] S. Narayana and Y. Sato, "Heat flux manipulation with engineered thermal materials," Phys. Rev. Lett. **108**, 214303 (2012).

[6] H. Y. Xu, X. H. Shi, F. Gao, H. D. Sun, and B. L. Zhang, "Ultrathin three-dimensional thermal cloak," Phys. Rev. Lett. **112**, 054301 (2014).

[7] T. C. Han, X. Bai, D. L. Gao, J. T. L. Thong, B. W. Li, and C. W. Qiu, "Experimental demonstration of a bilayer thermal cloak," Phys. Rev. Lett. **112**, 054302 (2014).

[8] Y. G. Ma, Y. C. Liu, M. Raza, Y. D. Wang, and S. L. He, "Experimental demonstration of a multiphysics cloak: Manipulating heat flux and electric current simultaneously," Phys. Rev. Lett. **113**, 205501 (2014).

[9] T. C. Han, X. Bai, J. T. L. Thong, B. W. Li, and C. W. Qiu, "Full control and manipulation of heat signatures: Cloaking, camouflage and thermal metamaterials," Adv. Mater. **26**, 1731 (2014).

[10] Y. Li, K. J. Zhu, Y. G. Peng, W. Li, T. Z. Yang, H. X. Xu, H. Chen, X. F. Zhu, S. H. Fan, and C. W. Qiu, "Thermal meta-device in analogue of zero-index photonics," Nat. Mater. **18**, 48 (2019).

[11] F. B. Yang, L. J. Xu, and J. P. Huang, "Thermal illusion of porous media with convection-diffusion process: Transparency, concentrating, and cloaking," ES Energy Environ. **6**, 45 (2019).

[12] Z. Y. Zhou, X. Y. Shen, C. C. Fang, and J. P. Huang, "Programmable thermal metamaterials based on optomechanical systems," ES Energy Environ. **6**, 85 (2019).

[13] R. Hu and X. B. Luo, "Two-dimensional phonon engineering triggers microscale thermal functionalities," Nat. Sci. Rev. **6**, 1071 (2019).

[14] X. He and L. Z. Wu, "Thermal transparency with the concept of neutral inclusion," Phys. Rev. E **88**, 033201 (2013).

[15] L. W. Zeng and R. X. Song, "Experimental observation of heat transparency," Appl. Phys. Lett. **104**, 201905 (2014).

[16] T. Z. Yang, X. Bai, D. L. Gao, L. Z. Wu, B. W. Li, J. T. L. Thong, and C. W. Qiu, "Invisible sensors: Simultaneous sensing and camouflaging in multiphysical fields," Adv. Mater. **27**, 7752 (2015).

[17] R. Z. Wang, L. J. Xu, Q. Ji, and J. P. Huang, "A thermal theory for unifying and designing transparency, concentrating and cloaking," J. Appl. Phys. **123**, 115117 (2018).

[18] S. Yang, L. J. Xu, and J. P. Huang, "Metathermotics: Nonlinear thermal responses of core-shell metamaterials," Phys. Rev. E **99**, 042144 (2019).

[19] S. Yang, L. J. Xu, and J. P. Huang, "Intelligence thermotics: Correlated self-fixing behavior of thermal metamaterials," Europhys. Lett. **126**, 54001 (2019).

[20] C. Su, L. J. Xu, and J. P. Huang, "Nonlinear thermal conductivities of core-shell metamaterials: Rigorous theory and intelligent application," Europhys. Lett. **130**, 34001 (2020).

[21] L. J. Xu and J. P. Huang, "Chameleonlike metashells in microfluidics: A passive approach to adaptive responses," Sci. China-Phys. Mech. Astron. **63**, 228711 (2020).

[22] A. P. Raman, M. A. Anoma, L. X. Zhu, E. Rephaeli, and S. H. Fan, "Passive radiative cooling below ambient air temperature under direct sunlight," Nature **515**, 540 (2014).

[23] P. Ben-Abdallah and S. A. Biehs, "Near-field thermal transistor," Phys. Rev. Lett. **112**, 044301 (2014).

[24] V. Kubytskyi, S. A. Biehs, and P. Ben-Abdallah, "Radiative bistability and thermal memory," Phys. Rev. Lett. **113**, 074301 (2014).

[25] S. A. Dyakov, J. Dai, and M. Yan, "Thermal radiation dynamics in two parallel plates: The role of near field," Phys. Rev. B **90**, 045414 (2014).

[26] S. A. Dyakov, J. Dai, M. Yan, and M. Qiu, "Near field thermal memory based on radiative phase bistability of VO_2," J. Phys. D: Appl. Phys. **48**, 305104 (2015).

[27] Z. Y. Li, "Optics and photonics at nanoscale: Principles and perspectives," Europhys. Lett. **110**, 1 (2015).

[28] R. Messina, W. L. Jin, and A. W. Rodriguez, "Exact formulas for radiative heat transfer between planar bodies under arbitrary temperature profiles: Modified asymptotics and sign-flip transitions," Phys. Rev. B **94**, 205438 (2016).

[29] Y. Zhai, Y. G. Ma, S. N. David, D. L. Zhao, R. N. Lou, G. Tan, R. G. Yang, and X. B. Yin, "Scalable-manufactured randomized glass-polymer hybrid metamaterial for daytime radiative cooling," Science **355**, 1062 (2017).

[30] J. Ordonez-Miranda, Y. Ezzahri, J. A. Tiburcio-Moreno, K. Joulain, and J. Drevillon, "Radiative thermal memristor," Phys. Rev. Lett. **123**, 025901 (2019).

[31] H. Y. Yu, H. C. Zhang, Z. N. Dai, and X. L. Xia, "Design and analysis of low emissivity radiative cooling multilayer films based on effective medium theory," ES Energy Environ. **6**, 69 (2019).

[32] Y. D. Liu, J. L. Song, W. X. Zhao, X. C. Ren, Q. Cheng, X. B. Luo, N. X. L. Fang, and R. Hu, "Dynamic thermal camouflage via a liquid-crystal-based radiative metasurface," Nanophotonics **9**, 855 (2020).

[33] J. L. Song, S. Y. Huang, Y. P. Ma, Q. Cheng, R. Hu, and X. B. Luo, "Radiative metasurface for thermal camouflage, illusion and messaging," Opt. Express **28**, 875 (2020).

[34]G. L. Dai, J. Shang, and J. P. Huang, "Theory of transformation thermal convection for creeping flow in porous media: Cloaking, concentrating, and camouflage," Phys. Rev. E **97**, 022129 (2018).
[35]G. L. Dai and J. P. Huang, "A transient regime for transforming thermal convection: Cloaking, concentrating and rotating creeping flow and heat flux," J. Appl. Phys. **124**, 235103 (2018).
[36]Y. Li, Y. G. Peng, L. Han, M. A. Miri, W. Li, M. Xiao, X. F. Zhu, J. L. Zhao, A. Alu, S. H. Fan, and C. W. Qiu, "Anti-parity-time symmetry in diffusive systems," Science **364**, 170 (2019).
[37]L. J. Xu and J. P. Huang, "Negative thermal transport in conduction and advection," Chin. Phys. Lett. **37**, 080502 (2020).
[38]L. J. Xu and J. P. Huang, "Controlling thermal waves with transformation complex thermotics," Int. J. Heat Mass Transf. **159**, 120133 (2020).
[39]J. Bear and M. Y. Corapcioglu, *Fundamentals of Transport Phenomena in Porous Media* (Springer, the Netherlands, 1984).
[40]See http://www.comsol.com/ for information about porous media module.
[41]J. Park, H. R. Youn, and Y. S. Song, "Hydrodynamic metamaterial cloak for drag-free flow," Phys. Rev. Lett. **123**, 074502 (2019).
[42]J. Park, J. R. Youn, and Y. S. Song, "Fluid-flow rotator based on hydrodynamic metamaterial," Phys. Rev. Appl. **12**, 061002 (2019).
[43]R. Hu, S. L. Zhou, Y. Li, D. Y. Lei, X. B. Luo, and C. W. Qiu, "Illusion thermotics," Adv. Mater. **30**, 1707237 (2018).
[44]Y. Li, X. Bai, T. Z. Yang, H. Luo, and C. W. Qiu, "Structured thermal surface for radiative camouflage," Nat. Commun. **9**, 273 (2018).
[45]R. Hu, S. Y. Huang, M. Wang, X. L. Luo, J. Shiomi, and C. W. Qiu, "Encrypted thermal printing with regionalization transformation," Adv. Mater. **31**, 1807849 (2019).
[46]J. X. Li, Y. Li, T. L. Li, W. Y. Wang, L. Q. Li, and C. W. Qiu, "Doublet thermal metadevice," Phys. Rev. Appl. **11**, 044021 (2019).
[47]X. Y. Peng and R. Hu, "Three-dimensional illusion thermotics with separated thermal illusions," ES Energy Environ. **6**, 39 (2019).
[48]B. W. Li, L. Wang, and G. Casati, "Thermal diode: Rectification of heat flux," Phys. Rev. Lett. **93**, 184301 (2004).
[49]Y. Li, X. Y. Shen, Z. H. Wu, J. Y. Huang, Y. X. Chen, Y. S. Ni, and J. P. Huang, "Temperature-dependent transformation thermotics: From switchable thermal cloaks to macroscopic thermal diodes," Phys. Rev. Lett. **115**, 195503 (2015).
[50]S. Y. Huang, J. W. Zhang, M. Wang, W. Lan, R. Hu, and X. B. Luo, "Macroscale thermal diode-like black box with high transient rectification ratio," ES Energy Environ. **6**, 51 (2019).
[51]G. W. Milton, *The Theory of Composites* (Cambridge University Press, Cambridge, 2004), Vol. 124.